Mechanical properties of single supramolecular polymers from correlative AFM and fluorescence microscopy

Mechanical Properties of Single Supramolecular Polymers from Correlative AFM and Fluorescence Microscopy

M.A. Beuwer, M.F. Knopper, L. Albertazzi, D. van der Zwaag, W.G. Ellenbroek, E.W. Meijer, M.W.J. Prins and P. Zijlstra

Abstract

AFM allows for the structural investigation of nanoscale objects, but statistical analysis is difficult when imaging fragile structures such as supramolecular polymers due to mechanical disruption by the AFM tip. Fluorescence microscopy on the other hand is non-invasive but lacks the resolution to reveal nanoscale features such as polymer entanglement and clustering. We show that correlation of AFM and fluorescence microscopy allows for the coupling of nanoscale morphological information to easily accessible far-field optical imaging, which we use for the reliable identification of clustering and entanglement based purely on diffraction limited fluorescence images. Using this correlative approach we analyze the persistence length of a fragile supramolecular polymer immobilized on a surface. By comparison with numerical simulations we find significant heterogeneity in the measured persistence length, which we attribute to polymer-substrate interactions and the presence of structural diversity within the polymer. This correlative approach paves the way to investigate statistical properties of fragile supramolecular structures.

Introduction

Supramolecular polymers are one-dimensional (1D) aggregates that self-assemble through non-covalent interactions, e.g. π-π stacking, hydrogen bonds, electrostatic and hydrophobic interactions (1). Biological supramolecular polymers, such as actin filaments and microtubules, are of major importance to cell structure, migration and differentiation (2). The unique properties of these biological polymers have sparked interest into bio-inspired supramolecular materials. These synthetic materials have been applied as biocompatible agents for drug delivery and scaffolds for tissue engineering (1,3-6), as self-healing additives that prevent misting and reduce drag in engines (7), and as semiconducting nanotubes in molecular electronics (1). These applications rely on the polymers' dynamic and responsive behaviour that arises due to the non-covalent nature of the monomer interactions.

Although the physical properties of polymers are in principle determined by the chemical structure of the monomer, the mechanical properties and dynamics of the polymer often remain difficult to predict from the monomer structure alone. For example, dynamic monomer exchange was thought to occur solely at the polymer's ends or through fragmentation-recombination, but recent reports revealed that monomer-exchange can also occur homogeneously along the polymer backbone (8,9).

The difficulty to predict polymer properties based on monomer structure has sparked efforts to characterize the physical properties of supramolecular polymers. Ensemble-averaged techniques such as UV-VIS spectroscopy (10,11), circular dichroism (10-13), and fluorescence emission (9) as well as small-angle X-ray scattering (SAXS) (14) have been applied.

Although these techniques give a wealth of information, single-polymer methods are able to discern rare states and reveal distributions of molecular properties instead of averages. Atomic force

microscopy (AFM) (15,16), cryo-electron microscopy (cryo-EM) (10,17) and confocal microscopy (18) are examples of techniques that have been used to characterize single supramolecular polymers. With these techniques the helical pitch and handedness of synthetic helical polymers was measured (15), a linear relation between the number of amyloid polymers in a fibril and its persistence length was revealed (16), the substituent-dependent formation of monolayers, bilayer ribbons or super-helical assemblies of J-aggregates was shown (17) and fiber growth and shrinkage over time was revealed (18). Although detailed structural information can be obtained with these techniques, acquisition of statistics is not straightforward because methods such as AFM and cryo-TEM are slow and can mechanically disrupt fragile structures. Microscopy on the other hand is diffraction limited and lacks the resolution to reveal nanoscale structure.

Recently, correlated microscopy approaches have been developed to tackle these issues. Correlated methods typically employ EM (19,20) or AFM (21-26) in combination with fluorescence microscopy to study one and the same structure. These methods benefit from the spatial resolution of EM and AFM, and the chemical specificity and throughput of fluorescence microscopy. Correlated EM and fluorescence microscopy has revealed that the morphology of individual growing microtubule plus-ends has a flared structure, i.e. the structure widens (19), and that nuclear pore complexes consist of subpopulations with different symmetries (20). Correlated AFM and fluorescence microscopy has also shown detailed topographical information about fluorescently labelled cytoskeleton proteins in cells (22,23) and the existence of multichromophoric polymers as both short non-helical oligomers and long helical polymers (24).

Here we use correlated fluorescence and atomic force microscopy (AFM) to study the structure and mechanical properties of single supramolecular polymers (10,27). Although these fragile structures are easily disrupted by mechanical interactions with the AFM tip, we show that correlation of AFM and fluorescence microscopy allows for the reliable identification of nanoscale features such as clustering and entanglement of polymers based purely on diffraction limited fluorescence images. We apply this correlative approach to study the persistence length of individual polymers and compare our results to numerical simulations based on the worm-like chain model. We analyze the distribution of single-polymer persistence lengths and discuss the underlying factors that induce inhomogeneous broadening.

Materials and methods

Synthesis and preparation of BTA polymers

We studied water-soluble 1,3,5-benzentricarboxamide (BTA) motifs with amphiphilic side-chains (Fig. 1a) that were synthesized and assembled as reported before (10). In short, BTA monomers (10) (Fig. 1a, R_1 = R_2 = -OH) and Cy5-labeled BTA monomers (8) (Fig. 1a R_1 = -OH, R_2 = -Cy5) were dissolved in methanol at a concentration of 10 mM and 1 mM, respectively. These solutions were subsequently mixed to obtain a ratio of Cy5-BTA to BTA of 0.02. The resulting solution in methanol was diluted in Milli-Q water to a final concentration of 25 μM. Dilution in Milli-Q water induces the self-assembly process through a combination of hydrophobic interactions and hydrogen bonds (Fig. 1b) (10). The diameter of these BTA polymers in solution was reported to be 6.2 nm using SAXS (28).

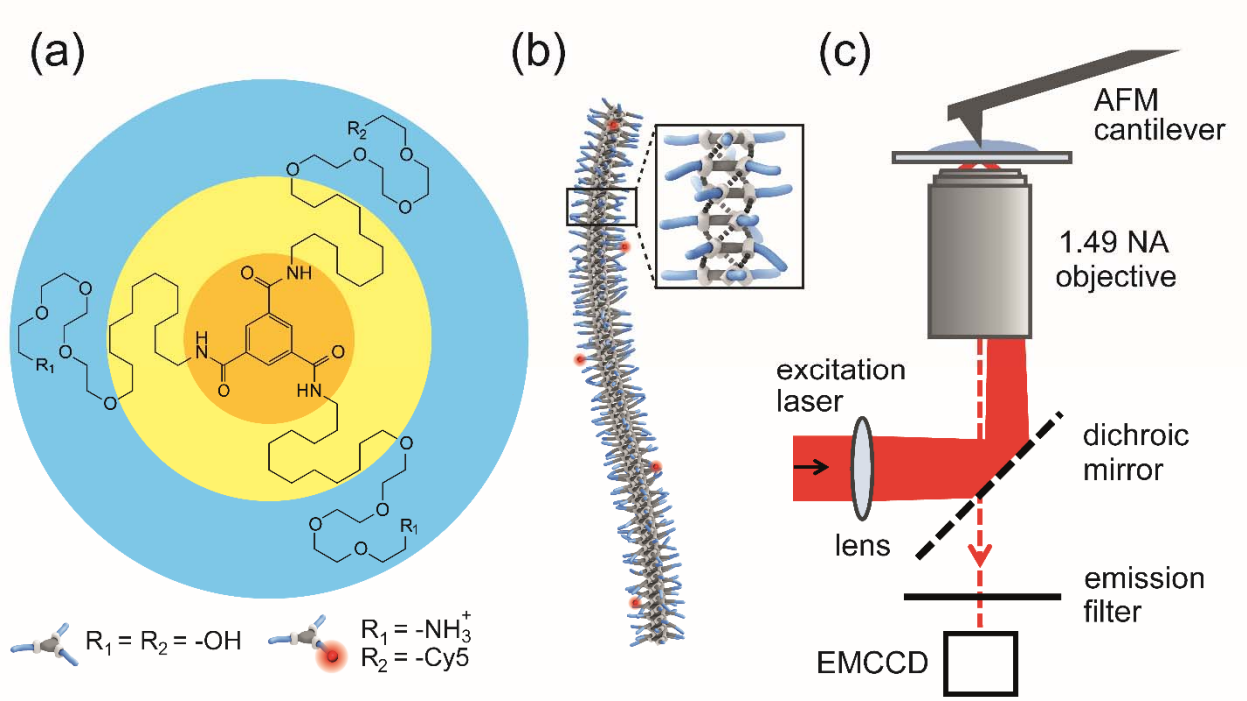

Fig. 1. Structure of water-soluble benzene-1,3,5-tricarboxamide (BTA) and experimental setup. (A) Chemical structure of BTA monomer. In a stack, the BTA core (orange) forms triple hydrogen bonds with neighbouring monomers. Three side-chains with alkane groups (yellow) give rise to hydrophobic interactions and polyethylene glycol (PEG) groups (blue) provide water-solubility. A fraction of the monomers (2%) is labelled with a fluorescent dye (Cy5). (B) Cartoon representation of a BTA polymer with Cy5-labeled monomers. Hydrogen bonds are illustrated by dashed lines in the inset. (C) Schematics of the setup.

Preparation of substrates

In our measurements BTA polymers were immobilized on glass substrates by physisorption. The coverslips (Menzel-Gläser, No. 1, 21×26 mm^2) were first sonicated in acetone, isopropanol and Milli-Q water for 5 minutes each, before incubating for 15 minutes in freshly prepared piranha etch (3:1 v/v H_2SO_4:H_2O_2 (30%)). Afterwards, the coverslips were sonicated in Milli-Q and acetone for 5 minutes each and dried under N_2-flow.

The solution of Cy5-BTA was further diluted to a monomer concentration of 5 µM using Milli-Q water. A droplet of diluted Cy5-BTA was dropcast on the piranha-etched coverslip and after 1 minute of incubation, unbound Cy5-BTA in solution was washed away with Milli-Q water. AFM and fluorescence microscopy experiments were performed in Milli-Q water. This preparation resulted in coverslips with several supramolecular polymers per field of view (100x100 μm^2), see Fig. 2.

Combined AFM and TIRF microscopy imaging

All experiments were performed with a combined total internal reflection fluorescence (TIRF) and atomic force microscopy (AFM) setup. A Bioscope Catalyst (Bruker Corporation, Massachusetts, USA) AFM was combined with a Ti Eclipse microscope (Nikon Corporation, Tokyo, Japan) by mounting the AFM stage on the microscope.

A home-built TIRF excitation beam path was used to excite the sample (Fig. 1c). The collimated light beam of a HeNe laser (632.8 nm, Thorlabs, Inc., New Jersey, USA) was directed to the objective (100x magnification, NA 1.49) via a dichroic mirror. Total internal reflection was achieved by placing a

tube lens off-centre with respect to the optical axis that focuses the beam in the back focal plane at the edge of the back aperture. The beam undergoes total internal reflection at the glass-water interface and the evanescent field excites the fluorescently-labelled BTA polymers. The reflected light was filtered out by the dichroic mirror and emission filter, and the emitted fluorescence was collected by an Andor iXon Ultra electron multiplying charged coupled device (EMCCD) camera (Andor Technology Ltd, Northern Ireland) with 1024x1024 pixel^2 resolution. An extra 1.5x magnification was used resulting in a pixel size of 87 nm in the object plane.

The AFM cantilever was manually aligned with the optical axis of the microscope using bright-field excitation from the top. Bruker AFM probes with 2 nm tip radius and cantilever stiffness ranging from 0.07 – 0.7 N/m were used for AFM imaging experiments. The AFM was operated in peak-force tapping mode, where the cantilever was modulated at a frequency of 1 kHz and the maximum force in the feedback loop was set to 200 pN. The advantage of peak-force tapping mode over tapping mode is its direct force control, making it well suited for topography measurements of biological and other soft samples. All combined TIRF and AFM measurements were performed in milliQ water.

Persistence length analysis

To extract the persistence length from fluorescence images we used an approach based on the cosine correlation function, where the apparent persistence length was analysed from skeletonized polymers (29). To prevent pixelation from influencing the shape of the backbone the image was interpolated. Furthermore, the polymer was deconvolved with a 2D Gaussian function with a full-width-at-half-maximum equal to the point spread function. On these deconvolved images skeletonization was performed by thresholding fluorescence images to create a binary image and eliminating the outer pixels of the backbone until a one-pixel wide skeleton remains. On these skeletonized polymers cosine correlation analysis was performed.

The cosine correlation function was used to analyse semi-flexible polymers that behave as a worm-like chain. The worm-like chain model uses a continuum description of the polymer to describe its mechanical properties. For a semi-flexible polymer the cosine correlation function is given by (29-31):

$$C(s) = \langle \cos[\theta(s_0 + s) - \theta(s_0)] \rangle_{s_0} = e^{-s/(2L_p)}, \quad (1)$$

where $\theta(s + s_0)$ is the tangent angle at coordinate $(s + s_0)$, $\theta(s_0)$ is the reference tangent angle and the average is taken over all reference points along the polymer. The persistence length is defined as the ratio of the bending stiffness κ and the thermal energy, $L_p = \kappa / k_B T$.

The coordinates along the polymer were determined from the skeletonized backbone which was first smoothed using a third-order Beziér spline fit. From this fit the tangent angles at each coordinate along the polymer were calculated. The cosine of the difference between tangent angles for different segment lengths s along the polymer contour length was calculated and averaged for each segment length. The cosine correlation function was then fitted to the averaged cosine correlation as a function of the segment length s. To prevent artefacts due to low sampling we only considered the cosine correlation function for s from 0 to 1 μm. A detailed explanation of the cosine correlation function is available in the Supporting Material.

Results and discussion

The fragile nature of the BTA polymers did not allow us to collect large numbers of AFM images that are needed for the statistical analysis of a persistence length. As shown in the Supporting Material (Fig. S6) interactions between the AFM tip and the polymer frequently led to damage and rupture of the molecules, even at the lowest forces that were accessible. With our correlative approach, we establish

an objective criterion to identify single and unentangled polymers directly from fluorescence images. We then used this criterion to determine the persistence length by collecting fluorescence images of many single molecules.

In Fig. 2 we show a typical fluorescence image of a sample showing several isolated supramolecular polymers. In typical images we observe not only polymer-like structures, but also a subpopulation that appears as a diffraction-limited spot. Of these polymer-like structures, a subpopulation (~30 %) exhibits large variations in fluorescence intensity along the backbone. Such intensity variations were observed to occur in extended regions along the polymer backbone, but were also sometimes localized to an area smaller than the diffraction limit. Unfortunately, the diffraction limit of conventional far-field microscopy is insufficient to resolve the structure of these polymers and also super-resolution techniques such as STORM have insufficient resolution to resolve polymers spaced by less than 10 nm (8). To trace the origin of the variations in intensity along the backbone, we correlated TIRF measurements with atomic force microscopy (AFM) in liquid to resolve the underlying topography.

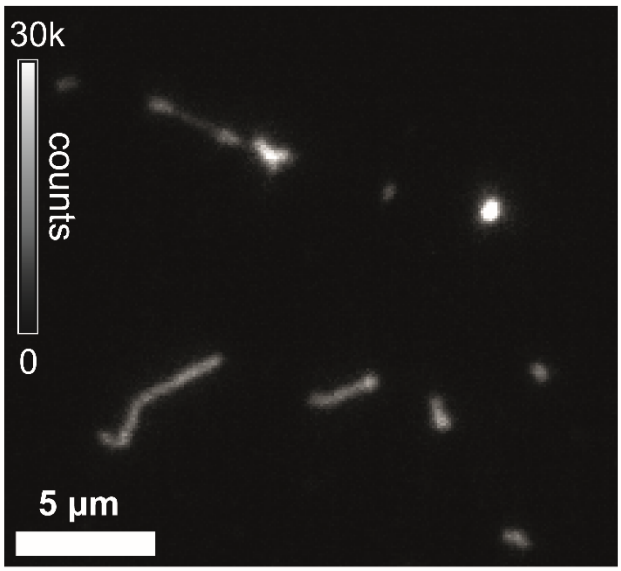

Fig. 2. Fluorescence image of immobilized BTA polymers. Bright spots correspond either to polymers that are smaller than the diffraction limit or to clusters of entangled polymers.

In Fig. 3 we show several examples of correlated AFM and fluorescence images of individual polymers. From a collection of AFM images we find that polymers exhibit heights ranging from 1.3 to 4.5 nm, whereas the width ranged from 11 to 27 nm (see Fig. S5 in the Supporting Material). The measured height is lower than the diameter of 6.2 nm obtained from SAXS measurements (28), and is most probably due to the compression of the side-chains by the force applied by the AFM probe (see Fig. S6 in the Supporting Material) or due to surface interactions that cause local differences in non-specific binding of the polymer to the glass surface. We find an average contour length of 7 ± 3 µm (n=83), in good agreement with previous studies (9,10).

In Fig. 3a-c we show a polymer that exhibits a uniform fluorescence intensity along its backbone. The AFM image reveals that this fluorescence signature corresponds to an individual and unentangled polymer. Approximately 60 % of the total analysed polymers fall in this category. In Fig. 3d-f, a brighter emission at the end of the polymer corresponds to an entangled chain, which were observed on ~30 % of analysed polymers. We also observe other nonuniform fluorescence intensities, ~5 % of cases correspond to multiple polymers that are spaced by less than the diffraction limit, see Fig. 3g-I, and

intertwined polymers were observed in ~5 % of cases, see Fig. 3j-l. Interestingly, in Fig. 3j we find several diffraction limited spots that correspond to one or more short polymers that are strongly entangled, see Fig. 3k. Because the resolution of both the AFM and fluorescence microscope are insufficient for a detailed analysis of such entangled polymers we focus in this study on the mechanical properties of single unentangled polymers.

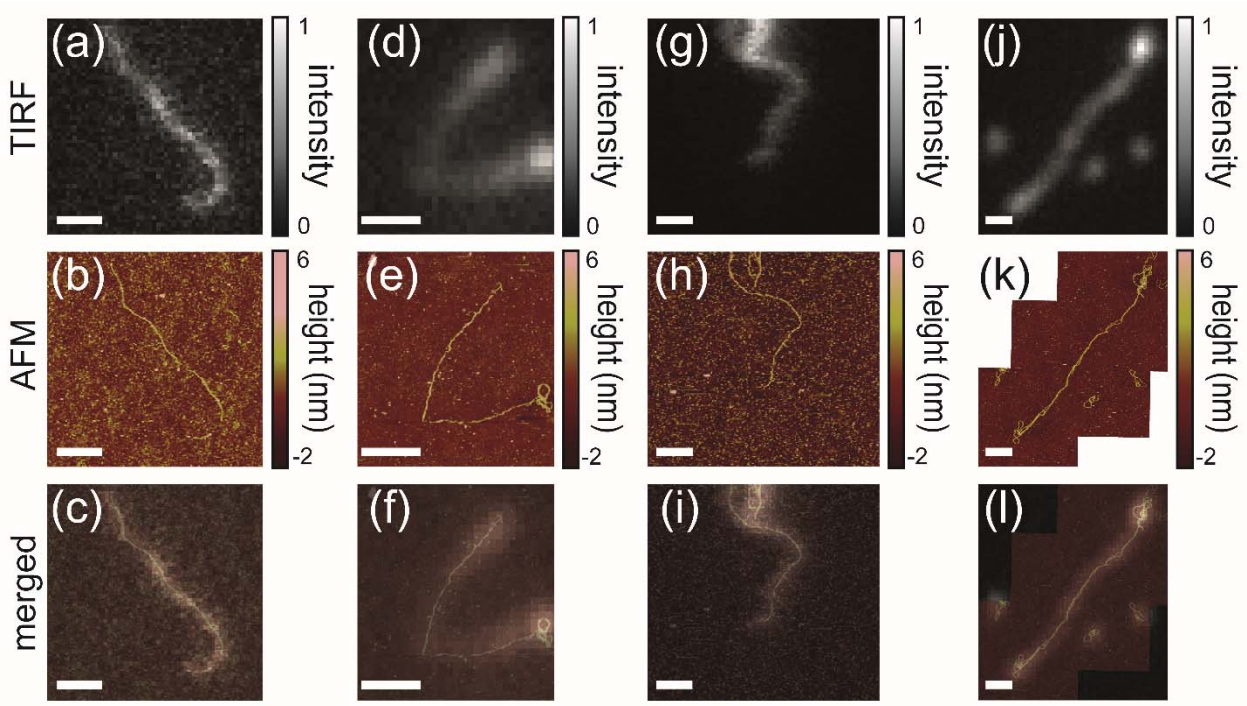

Fig. 3. Correlated AFM and TIRF images of BTA polymers. TIRF (a,d,g,j), AFM topography (b,e,h,k) and merged (c,f,l,j) images of individual BTA polymers. A homogenous intensity (a) corresponds to a single BTA polymer (b,c), whereas intensity variations (d,gi) correspond to entanglement or clustering (e,h,k). All scale bars are 1 µm.

It is yet unclear what causes these water-soluble BTA polymers to cluster or entangle, specifically at the polymer ends. It is likely that hydrophobic interactions play a role, either between side-chains or between the exposed core and side-chains. A mechanistic understanding of the origin of the entanglement could be obtained by e.g. studying polymers with hydrophobic regions with different lengths. Also, molecular dynamics simulations may provide direct molecular insight into the underlying causes of the observed morphology.

To obtain an objective criterion that allows for the identification of single and unentangled polymers from fluorescence images only, we analysed the emission intensity along the backbone of 84 supramolecular polymers, three examples are shown in Fig. 4. The top row shows the intensity profile along the BTA polymer shown in Fig. 3a-c, which is uniformly distributed as expected for an unentangled single polymer without interchain interactions that is homogeneously labelled. In Fig. 4e and f the intensity profile is shown for BTA polymers that exhibit regions with elevated emission intensity (Fig. 4b,c), giving rise to multimodal intensity distributions (Fig. 4h,i). Typically the peaks in the multimodal distributions are separated by an integer times the mean of the lowest-intensity part (x3 for Fig 4h, x2 for Fig 4i), thus suggesting the presence of an integer number of chains within the diffraction limited focal spot. Although a polymer that is intertwined along its whole length (Fig. 3j-l) cannot be identified by a nonuniform fluorescence intensity, we did not find any cases in which entangled ends were not also

observed. This suggests that identifying an intertwined polymer as a single entangled polymer is unlikely.

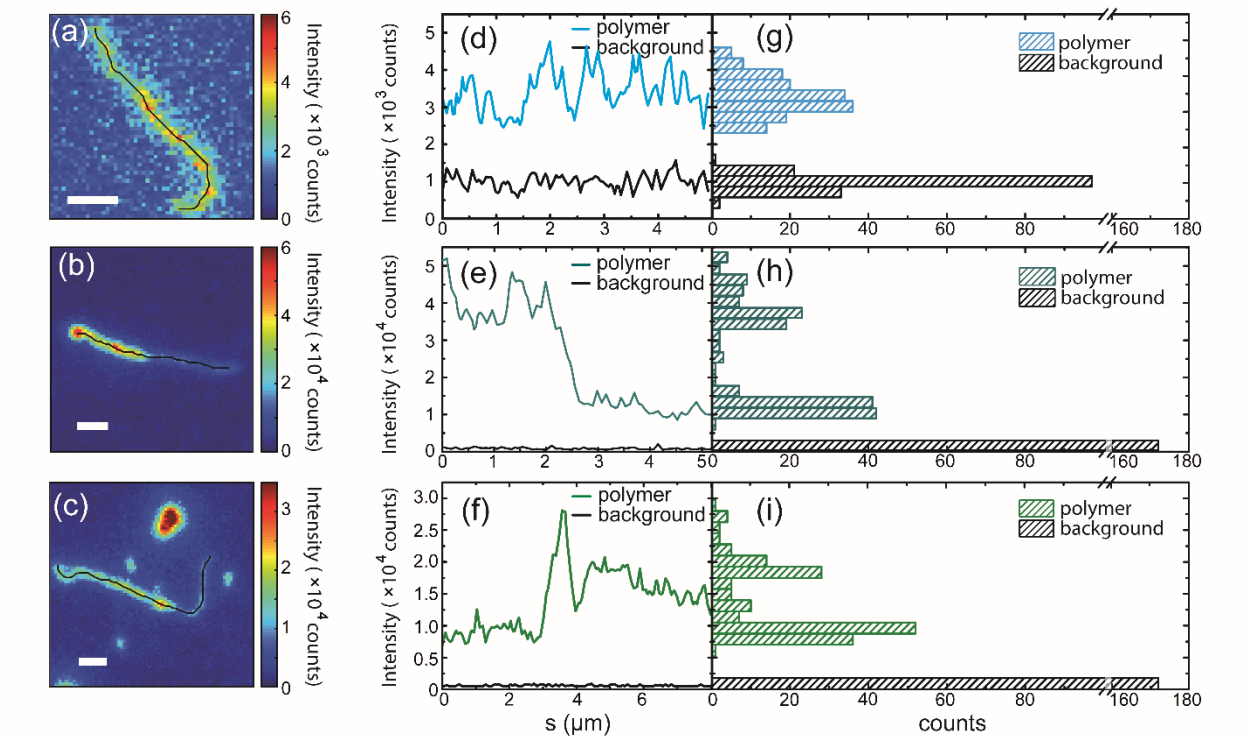

Fig. 4. Intensity distribution along the polymer backbone. The black lines in (a-c) represent the trajectory along which the intensity is plotted in (d-f). Scale bars are 1 μm. (d-f) Emission intensity along the backbone (blue, dark cyan and green lines) and background intensity (black lines). The background intensity was obtained by shifting the trajectory to a position next to the polymer. (g-i) Distributions of the polymer and background intensities. The difference in average intensity and background level arises due to varying exposure time and gain of the EMCCD camera.

To quantify the uniformity of the fluorescence intensity we use the ratio of the background-corrected standard deviation of the intensity to its mean, i.e. the coefficient of variation (CV). In Fig. 5 we show the distribution of this ratio for 84 polymers in a bee swarm plot and a histogram. We observe a broad range of CVs, with a concentration of data points around SV = 0.25 corresponding to single unentangled polymers. For the persistence length analysis we therefore exclude molecules with a CV > 0.4, corresponding to the sum of the mean and 2σ of the Gaussian fit in Fig 6. For comparison, the polymers shown in Fig. 3 exhibit a CV of 0.27 (Fig. 3a) and 0.54, 0.47 and 0.58 (Fig. 3d, g and j, respectively). Verification of a subset of 10 polymers using AFM imaging resulted in 100% correct assignment using the above criterion. The uniformity of the fluorescence intensity along the backbone of the polymer therefore provides a reliable criterion to identify single unentangled polymers, which we will use hereafter to study the polymer's mechanical properties.

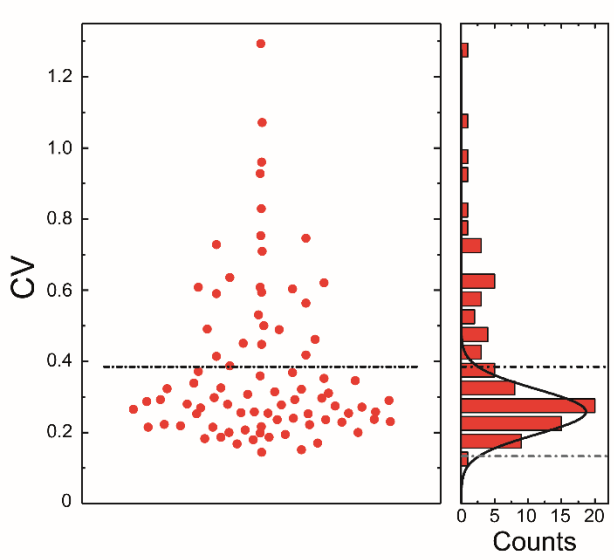

Fig. 5. Distribution of coefficient of variation (CV) of the intensity along all polymer backbones. For a CV above the threshold (the mean plus *2σ* of the plotted Gaussian fit), polymers are entangled or clustered and are excluded from persistence length analysis.

Persistence length analysis on single unentangled polymers

For a polymer that obeys worm-like-chain dynamics the persistence length is the length over which angular correlations decrease to $1/\sqrt{e}$ (for a polymer constrained in two dimensions). In literature, the persistence length has been determined using the end-to-end distance (32,33), cosine correlation analysis (30,34) or bending mode analysis (30). The latter determines the angular bending modes of a polymer through Fourier analysis. End-to-end analysis extracts the persistence length by fitting the relation between a polymer's end-to-end distance and its contour length. However, kinks along the polymer significantly influence the end-to-end distance and can cause bias in the persistence length.

In contrast, cosine correlation analysis uses the sum of *local* values (the bend angles) because it employs the angle between segments that are significantly shorter than the contour length. This yields significant statistics even for a single molecule and greatly reduces the bias caused by kinks. To extract the apparent persistence length from the cosine correlation function, an exponential decay (equation 1) was fitted to the correlation data. Note that in literature the bend angles for a certain segment length are often averaged over many polymers, followed by a fit with the cosine correlation function. It is then implicitly assumed that each polymer has the same persistence length, allowing for averaging of the bend angles before fitting. It is known that supramolecular polymers contain structural diversity (28) which might cause polymer-to-polymer variations in their persistence length. We therefore refrain from this pre-averaging and instead analyse the single-polymer data directly. This gives a value for the apparent persistence length for each separate polymer, of which we hen study the distribution.

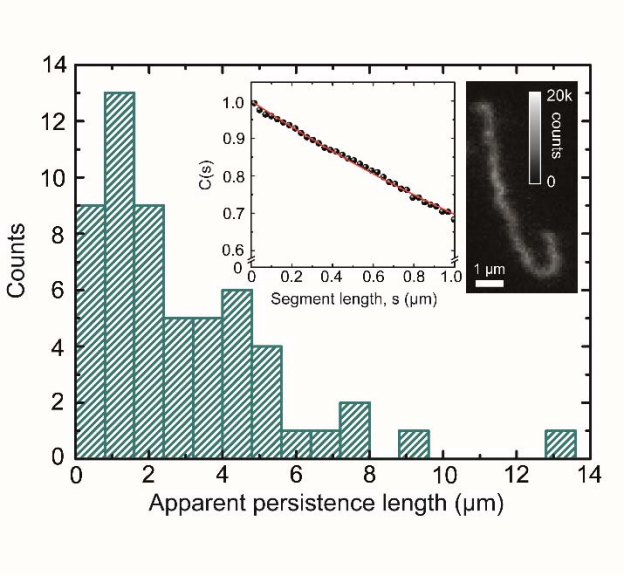

Fig. 6. Distribution of the apparent persistence lengths of single unentangled BTA polymers immobilized on glass. For each polymer the apparent persistence length is determined using cosine correlation analysis, where the cosine correlation is fitted with an exponential decay according to eq. (1) (inset). The apparent persistence length of the polymer shown in the inset is 1.39 ± 0.01 μm.

The distribution of apparent persistence lengths of unentangled single polymers is shown in Fig. 6. An example of the cosine correlation fit for one of the polymers is shown in the inset, yielding an apparent persistence length of 1.39 ± 0.01 μm. We observe a broad, positively skewed distribution of apparent persistence lengths with a clear peak between 1 – 1.5 μm. From the distribution we extract a median persistence length of 2.2 ± 1.4 μm (median ± median absolute deviation, MAD). The polymers that exhibited large fluorescence intensity variations due to clustering or entanglement exhibited a broad range of persistence lengths (see Fig. S7 in the Supporting Material). We speculate that clustering and entanglement may stiffen the polymer depending on the exact inter- and intramolecular interactions (35). The measured persistence length of 2.2 ± 1.4 μm is comparable to that of cofilin-bound actin filaments (38) and to amyloid-like fibrils (39) and in between the persistence lengths of well-known biopolymers such as ssDNA (2 nm) (36) and dsDNA (50 nm) (37), and actin (10 μm) (38) and microtubules (5.2 mm) (30) (see Fig. S8 in the Supporting Material).

Our analysis of single-molecule apparent persistence lengths uniquely obtains information on the shape and the width of the distribution. We further analyse the origins of the width of the measured distribution by comparing it to simulations.

Polymers with a persistence length of 1.5 μm (close to the measured value) were simulated using the worm-like chain model. We represented numerical worm-like chains as discrete jointed chains with straight segments of length Δs and angles between consecutive segments drawn from a normal distribution with variance $\Delta s/L_p$. The apparent persistence length for each polymer can then be calculated directly from the tangent angle at each coordinate along the polymer. A detailed explanation is available in the Supporting Material.

We analysed 100 simulated polymers by fitting the cosine correlation function directly to the computer-generated tangent angles. For polymers with a 1.5 μm persistence length we find a distribution of persistence lengths with a median ± MAD of 1.50 ± 0.31 μm. The uncertainty in the value arises from the limited length of each individual chain, leading to a different persistence length for each

computer-generated molecule. Nevertheless, the median persistence length is in good agreement with the expected value.

To better represent the experimental conditions, the simulated polymers were then convolved with a two dimensional Gaussian with a full-width-at-half-maximum (FWHM) equal to the diffraction-limited point spread function of our optical system, and subsequently pixelated. This resulted in polymers with the same resolution and pixelation as the fluorescence images measured. Background and shot noise were added as shown in Fig. S3 in the Supporting Material, yielding images with comparable signal-to-noise (~12) and signal-to-background (~3) ratios to our experimental images. After this procedure we find a persistence length of 1.80 ± 0.44 µm, see Fig 7a. The shift of the median of the distribution to longer persistence lengths and increased MAD are thus caused by the limited spatial resolution and the presence of noise (see Supporting Material). In Fig 7b we show the correlation between the persistence length obtained directly from the tangent angles, and the persistence length obtained after convolution, pixilation, and noise addition. We observe a strong correlation (R^2 = 0.97), with a slope of 1.18 ± 0.02, and a random deviation from the expected persistence length due to the shot noise. From these results it can be concluded that pixelation, convolution and noise somewhat increase the median persistence length, but more importantly, they considerably broaden the width of the distribution.

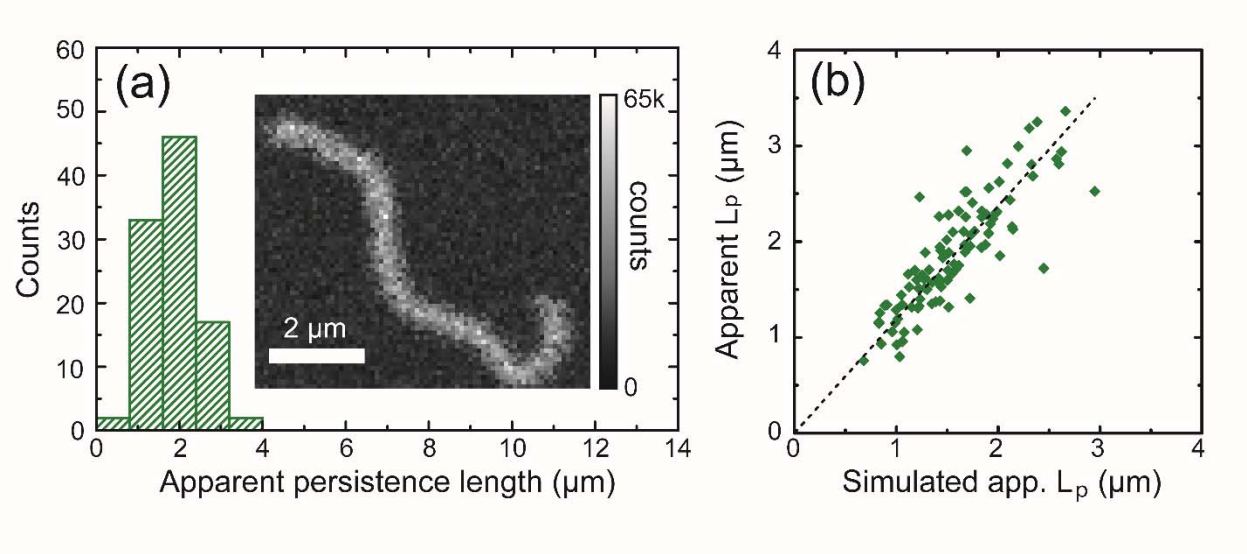

Fig. 7. Apparent persistence lengths for simulated polymers. (a) Distribution of apparent persistence lengths of simulated polymers that were pixelated and convolved with a 2D Gaussian to mimic experimental results. A persistence length of 1.80 ± 0.44 µm is found when polymers with a 1.5 µm persistence length were simulated. Inset: example of a computer-generated worm-like chain. (b) Correlation between apparent persistence lengths of the simulated polymer (obtained by direct fitting of the tangent angles) and the same polymer pixelated, convolved with a 2D Gaussian and with added noise.

Nevertheless, the width of our measured distribution is a factor of ~3 broader than expected from the pixelated and noisy simulated images, and exhibits a long tail toward longer persistence lengths. Below we discuss the possible origins of the broadening and tailing of the distribution.

First, polymer-to-polymer variations of the persistence length may inhomogeneously broaden the distribution. Recently, experiment (8) and theory (28) have hinted at the presence of structural variability due to imperfect stacking of monomers. This structural variability includes local bends and disorder in the structure of the polymer, which might result in stochastic variations of polymer diameter along the backbone. Starting from the definition of the persistence length $L_p = \kappa/k_BT$, where the

bending stiffness κ is the product of the shape independent material stiffness E and the second moment of area I (31,38), we find the relation between persistence length and polymer radius. For a cylinder with radius r the second moment of area is equal to $\frac{1}{4}\pi r^4$, which means $L_p \sim r^4$. Small changes in the radius would thus result in large changes in the persistence length.

Secondly, our analysis assumes that the polymers absorb onto the sample surface in a random conformation that is not influenced by the immobilization procedure and underlying sample topography. Although this has been shown to be true for specific samples (40,41), we cannot exclude that local flow and inhomogeneities of the underlying substrate (e.g. local differences in charge density after piranha etching) affect the conformation of the absorbed molecule. To minimize these effects we excluded areas on the sample where neighbouring polymers were clearly aligned (see Fig. S4 in the Supporting Material). It is however possible that a fraction of polymers were less visibly affected by for example flow, resulting in a tail towards longer persistence lengths. Future studies on polymers that are not immobilized but freely diffuse in solution between two tightly spaced substrates might be used to quantify these effects.

Conclusions

In conclusion, we have shown the application of correlative microscopy to study the mechanical properties of supramolecular polymers. Atomic force microscopy revealed that a fraction of polymers were in a clustered or entangled state. The fragility of the supramolecular polymers did not allow us to reliably measure their persistence length using AFM. However, correlation with fluorescence microscopy allowed us to identify single and unentangled polymers purely based on the emission intensity along the backbone. Thus, this correlative technique facilitates the analysis of statistical properties of fragile supramolecular polymers.

For these single and unentangled polymers we found a persistence length of 2.2 ± 1.4 μm by cosine correlation analysis. Few fully atomistic calculations on supramolecular polymers in water have been performed, except for peptide amphiphiles. Molecular dynamics simulations on cyclic peptide nanotubes (42) and β-sheet filaments (43) yielded persistence lengths of 0.46 μm and 1.2 – 4.8 μm, respectively, comparable to our measured value for BTA.

Comparison of the distribution of apparent persistence lengths with simulations revealed that the measured distribution was significantly broader than expected. We suggest that this broadening might be caused by a distribution of intrinsic persistence lengths, or by the immobilization of the molecules where local flow or surface inhomogeneities might play a role. Our analysis shows the advantages of studying single-polymer (apparent) persistence lengths, which not only allows for the comparison of the average values to simulations but also maintains information on the shape and width of the distribution.

Supporting Material

Supporting Material and Methods, and eight figures are available as supplementary information.

Author contributions

M.A.B. and M.F.K. performed the fluorescence microscopy experiments. M.A.B. performed AFM and correlative experiments and wrote the code to analyse the data. W.G.E. generated the worm-like chains using molecular dynamics. L.A. and D.v.d.Z. supplied the BTA molecules, assisted in fluorescence microscopy experiments and gave input on data interpretation, and M.W.J.P., E.W.M. and P.Z. supervised the work. The article was written by M.A.B. with input from all authors.

Acknowledgements

We thank Dr. Kees Storm for his kind help with regard to the molecular dynamics calculations to generate worm-like chains. We like to thank the Dutch Ministry of Education, Culture and Science for their support (Gravity program 024.001.035). This work was supported by NWO Vidi grant 680-47-530 from the Netherlands Organization for Scientific Research.

References

1 Aida, T., E.W. Meijer, and S.I. Stupp. 2012. Functional supramolecular polymers. *Science* 335:813–817

2 Fletcher, D.A. and R.D. Mullings. 2010. Cell mechanics and the cytoskeleton. *Nature* 463:485-492

3 Dong, R., Y. Zhou, X. Huang, X. Zhu, Y. Lu, and J. Shen. 2015. Functional supramolecular polymers for biomedical applications. *Adv. Mater.* 27:498-526.

4 Boekhoven, J. and S.I. Stupp. 2014. 25th anniversary article: supramolecular materials for regenerative medicine. *Adv. Mater.* 26:1642-1659.

5 Busserson, E., Y. Ruff, E. Moulin, and N. Guiseppone. 2013. Supramolecular self-assemblies as functional nanomaterials. *Nanoscale* 5:7098-7140.

6 Bakker, M.H., C.C. Lee, E.W. Meijer, P.Y.W. Dankers, and L. Albertazzi. 2016. Multicomponent polymers as a modular platform for intracellular delivery. *ACS Nano* 10: 1845-1852.

7 Wei, M-H., B. Li, R.L. Ameri David, S.C. Jones, V. Sarohia, J.A. Schmitigal, and J.A. Kornfield. 2015. Megasupramolecules for safer, cleaner fuel by end association of long telechelic polymers. *Science* 350:72-75.

8 Albertazzi, L., D. van der Zwaag, C.M.A. Leenders, R. Fitzner, R.W. van der Hofstad, and E.W. Meijer. 2014. Probing exchange pathways in one-dimensional aggregates with super-resolution microscopy. *Science* 344:491-495.

9 Albertazzi, L., F.J. Martinez-Veracoechea, C.M.A. Leenders, I.K. Voets, D. Frenkel, and E.W. Meijer. 2013. Spatiotemporal control and superselectivity in supramolecular polymers using multivalency. *Proc. Natl. Acad. Sci. USA* 110:12203-12208.

10 Leenders, C.M.A., L. Albertazzi, T. Mes, M.M.E. Koenigs, A.R.A. Palmans, and E.W. Meijer. 2013. Supramolecular polymerization in water harnessing both hydrophobic effects and hydrogen bond formation. *Chem. Commun.* 49:1963–1965.

11 Schenning, A.P.H.J., P. Jonkheijm, E. Peeters, and E.W. Meijer. 2001. Hierarchical order in supramolecular assemblies of hydrogen-bonded oligo(p-phenylene vinylene)s. *J. Am. Chem. Soc.* 123:409-416.

12 Palmans, A.R.A. and E.W. Meijer. 2007. Amplification of chirality in dynamic supramolecular aggregates. *Angew. Chem. Int. Ed.* 46:9849-8969.

13 Korevaar, P.A., S.J. George, A.J. Markvoort, M.M.J. Smulders, P.A.J. Hilbers, A.P.H.J. Schenning, T.F.A. de Greef, and E.W. Meijer. 2012. Pathway complexity in supramolecular polymerization. *Nature* 481:492-497.

14 Besenius, P., G. Portale, P.H.H. Bomans, H.M. Janssen, A.R.A. Palmans, and E.W. Meijer. 2010. Controlling the growth and shape of chiral supramolecular polymers in water. *Proc. Natl. Acad. Sci. USA* 107:17888-17893.

15 Kumaki, J., S-i. Sakurai, and E. Yashima. 2009. Visualization of synthetic helical polymers by high-resolution atomic force microscopy. *Chem. Soc. Rev.* 38:737-746.

16 Adamcik, J., J. Jung, J. Flakowski, and R. Mezzenga. 2010. Understanding amyloid aggregation by statistical analysis of atomic force microscopy images. *Nat. Nanotechnol.* 5:423-428.
17 Von Berlepsch, H., C. Böttcher, A. Ouart, C. Burger, S. Dähne, and S. Kirstein. 2000. Supramolecular structures of J-aggregates of Carbocyanine dyes in solution. *J. Phys. Chem. B* 104:5255-5262.
18 Boekhoven, J., W.E. Hendriksen, G.J.M. Koper, R. Eelkema, and J.H. van Esch. 2015. Transient assembly of active materials fueled by a chemical reaction. *Science* 349:1075-1079.
19 Kukulski, W., M. Schorb, S. Welsch, A. Picco, M. Kaksonen, and J.A.G. Briggs. 2011. Correlated fluorescence and 3D electron microscopy with high sensitivity and spatial precision. *J. Cell Biol.* 192:111-119.
20 Löschberger, A., C. Franke, G. Krohne, S. van de Linde, and M. Sauer. 2014 Correlative super-resolution fluorescence and electron microscopy of the nuclear pore complex with molecular resolution. *J. Cell Sci.* 127:4351-4355.
21 Vickery, S.A. and R.C. Dunn. 2001. Combining AFM and FRET for high resolution fluorescence microscopy. *J. Microsc.* 292:408-412.
22 Kellermayer, M.S.Z., A. Karsai, A. Kengyel, A. Nagy, P. Bianco, T. Huber, A. Kulcsar, C. Niedetzky, R. Proksch, and L. Grama. 2006. Spatially and temporally synchronized atomic force and total internal reflection fluorescence microscopy for imaging and manipulating cells and biomolecules. *Biophys. J.* 91(7):2665-2677.
23 Chacko, J.V., F.C. Zanacchi, and A. Diaspro. 2013. Probing cytoskeletal structures by coupling optical superresolution and AFM techniques for a correlative approach. *Cytoskeleton* 70:729-740.
24 Hernando, J., P.A.J. de Witte, E.M.H.P. van Dijk, J. Korterik, R.J.M. Nolte, A.E. Rowan, M.F. García-Parajó, and N.F. van Hulst. 2004. Investigation of perylene photonic wires by combined single-molecule fluorescence and atomic force microscopy. *Angew. Chem. Int. Ed.* 43:4045-4049.
25 Micic, M., D. Hu, Y.D. Suh, G. Newton, M. Romine, and H.P. Lu. 2004. Correlated atomic force microscopy and fluorescence lifetime imaging of live bacterial cells. *Colloids Surf. B Biointerfaces*, 34(4):205–212.
26 Noy, A. and T.R. Huser. 2003. Combined force and photonic probe microscope with single molecule sensitivity. *Rev. Sci. Instrum.* 74:1217-1221.
27 Cantekin, S., T.F.A. de Greef, and A.R.A. Palmans. 2012. Benzene-1,3,5-tricarboxamide: a versatile ordering moiety for supramolecular chemistry. *Chem. Soc. Rev.* 41:6125–6137.
28 Baker, M.N., L. Albertazzi, I.K. Voets, C.M.A. Leenders, A.R.A. Polmans, G.M. Pavan, and E.W. Meijer. 2015. Consequences of chirality on the dynamics of a water-soluble supramolecular polymer. *Nature Commun.* 6:6234.
29 Graham, J.S., B.R. McCullough, H. Kang, W.A. Elam, W. Cao, and E.M. De La Cruz. 2014. Multi-platform compatible software for analysis of polymer bending mechanics. *PLoS One* 9(4):e94766.
30 Gittes, F., B. Mickey, J. Nettleton, and J. Howard. 1993 Flexural rigidity of microtubules and actin filaments measured from thermal fluctuations in shape. *J. Cell Biol.* 120:923-934.
31 Broedersz, C.P. and F.C. MacKintosh. 2014. Modeling semiflexible polymer networks. *Rev. Mod. Phys.* 86:995-1036.
32 Howard, J. 2001. *Mechanics of motor proteins and the cytoskeleton.* Sunderland, MA, Sinauer Associates, Inc.
33 Landau, L.D. and E.M. Lifshitz. 1980. *Statistical physics 3rd edition, Part 1*. Butterworth-Heinemann
34 Isambert, H., P. Venier, A.C. Maggs, A. Fattoum, R. Kassab, D. Pantaloni, and M.F. Carlier. 1995. Flexibility of actin filaments derived from thermal fluctuations. Effect of bound nucleotide, phalloidin and muscle regulatory proteins. *J. Biol. Chem.* 270:11437-11444.
35 Kouwer, P.H.J., M. Koepf, V.A.A. le Sage, M. Jaspers, A.M. van Buul, Z.H. Eksteen-Akeroyd, T. Woltinge, E. Schwartz, H.J. Kitto, R. Hoogenboom, S.J. Picken, R.J.M. Nolte, E. Mendes, and A.E.

Rowan. 2013. Responsive biomimetic networks from polyisocyanopeptide hydrogels. *Nature* 493: 651-655.

36 Murphy, M.C., I. Rasnik, W. Cheng, T.M. Lohman, and T.J. Ha. 2004. Probing single-stranded DNA conformational flexibility using fluorescence spectroscopy. *Biophys. J.* 86:2530-2537.

37 Hagerman, P.J. 1988. Flexibility of DNA. *Ann. Rev. Biophys. Biophys. Chem.* 17:265-86.

38 McCullough, B.R., L. Blanchoin, J-L. Mariel, and E.M. De La Cruz. 2008. Cofilin increases the bending flexibility of actin filaments: implications for severing and cell mechanics. *J. Mol. Biol.* 381:550-558.

39 Bortolini, C., N.C. Jones, S.V. Hoffman, C. Wang, F. Besenbacher, and M. Dong. 2015. Mechanical properties of amyloid-like fibrils defined by secondary structures. *Nanoscale* 7:7745-7752.

40 Abels, J.A., F. Moreno-Herrero, T. van der Heijden, C. Dekker, and N.H. Dekker. 2005. Single-molecule measurements of the persistence length of double-stranded RNA. *Biophys. J.* 88:2737-2744.

41 Rivetti, C., M. Guthold, and C. Bustamante. 1996. Scanning force microscopy of DNA deposited onto mica: equilibrium versus kinetic trapping studied by statistical polymer chain analysis. *J. Mol. Biol.* 264: 919-932.

42 Ruiz, L., P. von Achen, T.D. Lazzara, T. Xu, and S. Keten. 2013. Persistence length and stochastic fragmentation of supramolecular nanotubes under mechanical force. *Nanotechnology* 24:195103.

43 Park, J., B. Kahng, R.D. Kamm, and W. Hwang. 2006. Atomistic simulation approach to a continuum description of self-assembled β-sheet filaments. *Biophys. J.* 90:1510-2524.

Supplementary information

Mechanical Properties of Single Supramolecular Polymers from Correlative AFM and Fluorescence Microscopy

M.A. Beuwer, M.F. Knopper, L. Albertazzi, D. van der Zwaag, W.G. Ellenbroek, E.W. Meijer, M.W.J. Prins and P. Zijlstra

Table of Contents

Introduction on quantifying persistence length

Inextensible polymers that exhibit a resistance to bending are usually described with the worm-like chain model (1). The key parameter of this model is the bending stiffness κ. Describing the position along the polymer chain (length L) with a coordinate $s \in (0, L)$, measured along the polymer backbone, $\vec{r}(s)$ is the position of a chain segment and $\hat{t}(s) = {d\vec{r}}/{ds}$ is a unit tangent vector denoting the local orientation.

The key physics of the bending resistance is captured in the model by introducting an energy penalty on gradients of $\hat{t}(s)$, given by

$$E_{\text{bend}} = \frac{\kappa}{2} \int ds \left| \frac{d\hat{t}}{ds} \right|^2, \tag{S1}$$

so that higher bending moduli lead to straighter chains. The combined effect of thermal fluctuations and bending stiffness then leads to a typical length (measured along the backbone) over which the chain orientation decorrelates, the persistence length $L_p = \kappa/(k_B T)$. This length can be extracted from any form of data that describes the local orientation of the polymer chain as a function of contour length *s*, by fitting the tangent vector autocorrelation to its theoretical prediction (2):

$$C(s) = \langle \hat{t}(s) \cdot \hat{t}(0) \rangle = \exp\left[-\frac{s}{2l_p} \right]. \tag{S2}$$

Here the average is taken over an ensemble of similar chains. The factor 2 in this equation is only present for chains adsorbed onto a flat surface, as we study in this paper. In adsorbed chains, the tangent vector can be represented with a single angle $\theta(s)$ indicating the angle between $\hat{t}(s)$ and a chosen reference axis in the plane of the surface, and the average can be rewritten as $C(s) = \langle \cos[\theta(s) - \theta(0)] \rangle$. We therefore refer to $C(s)$ as the *cosine correlation function*.

Persistence length analysis

In order to find the persistence length of adsorbed two-dimensional semi-flexible polymers the tangent angles at coordinates along the polymer are calculated from the polymer backbone. From these tangent angles the apparent persistence length is calculated for each polymer using cosine correlation analysis.

The polymer backbone of each polymer was obtained by pre-processing the raw image of the polymers (Fig. 1a) using the free image-processing software *ImageJ* based on a similar approach as Graham *et al* (3). Using thresholding and skeletonization (Fig. 1d), i.e. creating a one-pixel-wide backbone by eliminating the outer pixels of the polymer, the polymer backbone can be analysed using our persistence length analysis script. However, due to pixelation the polymer backbone doesn't always follow the polymer, because the pixel size is large compared to the width of the polymer. This created curvature in the backbone that is not present in the polymer, therefore prior to thresholding images were interpolated with a factor 9, i.e. each pixel is divided into nine subpixels, where each subpixel is given a weighted intensity of its nearest neighbours (Fig. 1b). To further improve localization of the polymer backbone the polymer was deconvolved with a 2D Gaussian with the FWHM of the experimental point spread function (Fig. 1c). Before thresholding and skeletonization, the image was Gaussian-smoothed to improve thresholding. The Gaussian smoothing was necessary to smooth inhomogeneities in the intensity caused by deconvolution of a noisy image, the Gaussian kernel used was however much smaller than the 2D Gaussian used for devonvolution.

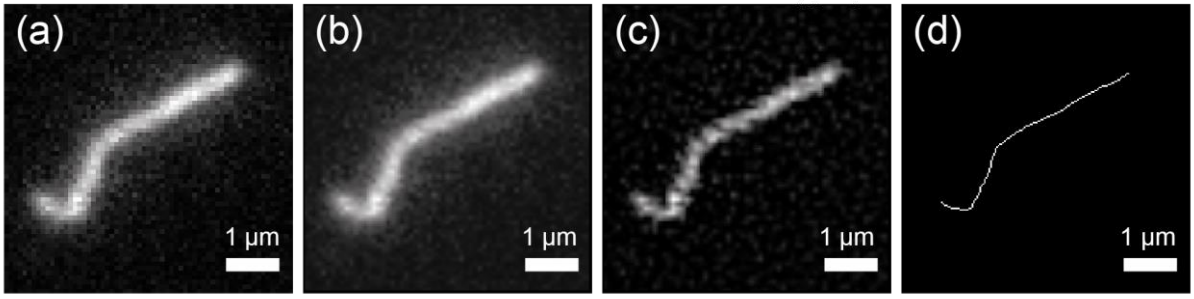

Fig. S1. Pre-processing of the raw image to extract the polymer backbone. The raw image of a polymer (a) is pre-processed by enhancing contrast and interpolation (b) to improve the shape of the final one-pixel-wide backbone. The polymer is deconvolved with a 2D Gaussian to decrease its width (c) and is finally thresholded and skeletonized, resulting in a one-pixel-wide polymer backbone (d).

The backbone coordinates are then smoothed by fitting a third-order Beziér spline using Matlab (The MathWorks Inc., Natick, MA). For each coordinate along the reconstructed polymer, the tangent angle is calculated and from these tangent angles the cosine correlation, as defined below, is calculated.

The persistence length is calculated by fitting the cosine correlation function for two-dimensional (2D) fluctuations (equation S3) to the averaged cosine correlation values. When applied to a single immobilized polymer an apparent persistence length is obtained, as the polymer is in one of infinite configurations. Only when performing cosine correlation on many configurations of one polymer or many of the same polymer the persistence length is obtained.

Simulated polymers using the worm-like chain model

In this paper, we use the term "apparent persistence length" to describe the persistence length of a single adsorbed polymer. This quantity is obtained by fitting an exponential function to the cosine correlation function usually used to describe the ensemble-average persistence of many chains with the same underlying bending stiffness κ. With the definition $L_p = \kappa/(k_B T)$, we have, for a chain adsorbed on a surface (1),

$$C(s) = \langle \cos[\theta(s + s_0) - \theta(s_0)] \rangle_{s_0} = e^{-s/(2l_p)}. \quad \text{(S3)}$$

Here, we average only over different starting points s_0 along the same chain, resulting in a single-chain apparent persistence length. The fitting procedure focuses on small values of s, as this procedure provides poor statistics for $s > 0.1L$.

In order to relate the distributions of these apparent persistence lengths to the underlying persistence length (intrinsic bending stiffness) of the experimental polymers, we need to know how they are influenced by noise and other experimentally unavoidable limitations to accuracy. To this end we employ a sample of computer-generated worm-like chains with an underlying (ensemble-averaged) persistence length of $L_p = 1.5\ \mu\text{m}$, and analysed them with the same procedure used to analyse the TIRF-images from our experiments.

We represent numerical worm-like chains as discrete jointed chains with straight segments of length Δs and angles between consecutive segments drawn from a normal distribution with variance $\Delta s/L_p$ (see Fig. S2). This procedure amounts to discretizing the integral in equation (S1) and applying the equipartition theorem. These angles uniquely determine the shape of the adsorbed chain. We can calculate the exact cosine correlation function of this model because it is written in terms of the same angle $\theta(s)$ that defines this correlation. Thus, we have precise values for the apparent persistence length of these chains, the distribution of which we can compare to experiments.

The sample used to generate Figure 7 in the main text consisted of 100 worm-like chains of length $10\ \mu\text{m}$, represented using 400 segments of length 25 nm (which is below the pixel size for all subsequent analyses). An example is shown in Figure S2.

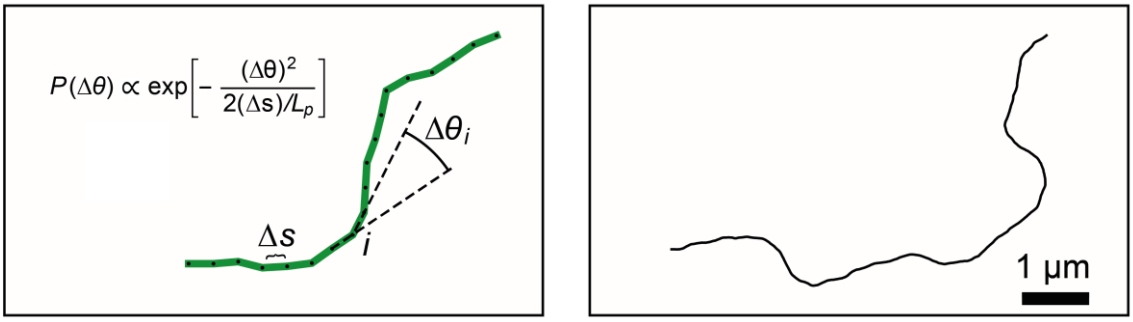

Fig. S2. Simulated polymer using the worm-like chain model. (a) Fragment of simulated polymer with $\Delta s = 20\ \mu\text{m}$ showing the angles between $\Delta\theta_i$ between segments. (b) Simulated worm with a 1.5 µm persistence length, a contour length of 10 µm and $\Delta s = 25\ \text{nm}$.

These simulated polymers were convolved with a two dimensional Gaussian with a full-width-at-half-maximum (FWHM) equal to the diffraction-limited point spread function of our optical system. This resulted in polymers with the same pixelation and resolution as the fluorescence images of the BTA polymers. Background Poisson noise was added to mimic the readout noise of the EMCCD together with Poisson noise to mimic shot noise. This resulted in images with comparable signal-to-noise (~12.2) and signal-to-background (~2.5) ratios to our experimental images.

Poissonian noise was generated using the rejection method, a technique to generate random deviates from a known and computable distribution function *p(x)dx* (4). The rejection method requires a continuous distribution, whereas the Poisson distribution

$$\mathrm{Prob}(j) = \int_{j-\epsilon}^{j+\epsilon} p_x(m)dm = \frac{x^j e^{-x}}{j!}, \tag{S4}$$

where *j* is the number of events occurring in an interval *x*, is discrete. This results in a distribution function that is zero everywhere, except where *m* is an integer larger or equal to zero. By defining a continuous distribution

$$q_x\,(m)dm = \frac{x^{[m]}e^{-x}}{[m]!}\,dm, \tag{S5}$$

where *[m]* is the largest integer less than *m*, the rejection method can be used. Now when a noninteger deviate is generated, it is rounded to the next lower integer part and from this deviate a random number is drawn from the Poisson distribution.

Persistence length analysis of simulated polymers

100 polymers with a 1.5 µm persistence length were simulated using the worm-like chain model. From the generated angles the apparent persistence length were calculated using cosine correlation analysis. The resulting distribution is shown in Fig. S3a and yields a persistence length of 1.50 ± 0.31 µm (median ± median absolute deviation, MAD). In order to compare simulations to experiments, polymers with the same pixelation and diffraction-limited resolution were generated by convolving the simulated polymers with a 2D Gaussian with a FWHM equal to the experimental point spread function. Persistence length analysis of convolved and pixelated polymers yielded the distribution of apparent persistence lengths shown in Fig. S3b. The resulting persistence length is 1.64 ± 0.36 µm, showing an increase in persistence length and slight broadening of the distribution. This shift and broadening both increase when shot noise is added to the images to accurately mimic the experimental images. The distribution of apparent persistence lengths yields a persistence length of 1.80 ± 0.44 µm, which means convolution and pixelation with added shot noise results in a 0.3 µm increase in persistence length compared to the persistence length of the simulated polymers, where both the convolution and pixelation and the added noise contribute equally to the increase.

In Fig. S3d and e the apparent persistence lengths of the 100 simulated polymers are correlated to the convolved and pixelated polymers (d) and the same polymers with shot noise (e). Both show excellent correlation and linear fits with a slope of 1.10 ± 0.01 (d) and 1.18 ± 0.02 (e) again reveal the increase in apparent persistence length.

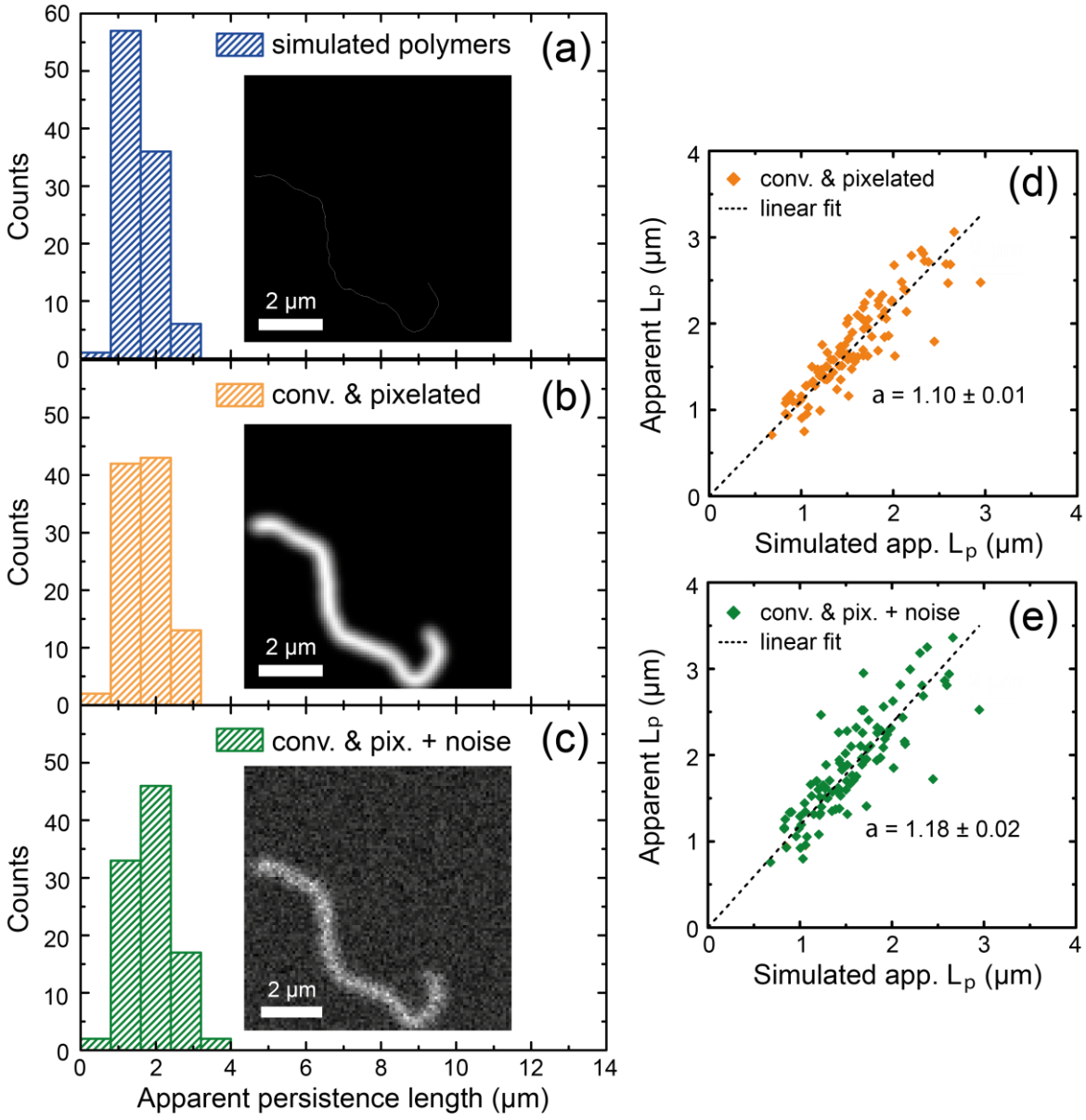

Fig. S3. Results of persistence length analysis of simulated polymers. (a) Distribution of apparent persistence lengths of simulated polymers. The apparent persistence length is directly calculated from the generated angles at the coordinate along the polymer, yielding a persistence length of 1.50 ± 0.31 µm. Inset: simulated polymer with a contour length of 10 µm and a 1.5 µm persistence length. (b) Distribution of apparent persistence lengths of pixelated simulated polymers convolved with a 2D Gaussian yields a persistence length of 1.64 ± 0.36 µm. Inset: convolved and pixelated polymer. (c) Distribution of apparent persistence lengths of convolved and pixelated polymer with added shot noise yield a persistence length of 1.80 ± 0.44 µm. Inset: convolved and pixelated polymer with added shot noise. (d) Correlation of apparent persistence lengths of 100 simulated polymers with the convolved and pixelated version of the same polymer. A linear fit yields a slope *a* of 1.10 ± 0.01. (e) Correlation of apparent persistence lengths of 100 simulated polymers with the convolved and pixelated version with added shot noise of the same polymer. A linear fit yields a slope *a* of 1.18 ± 0.02.

Immobilized BTA polymers experiencing flow

Some polymers experienced local flow, evident from the fact that multiple polymers were aligned and stretched in the same direction (Fig. S3). These were excluded from persistence length analysis by eye, where the criterion was that flow was present when two or more polymers were aligned in the same direction.

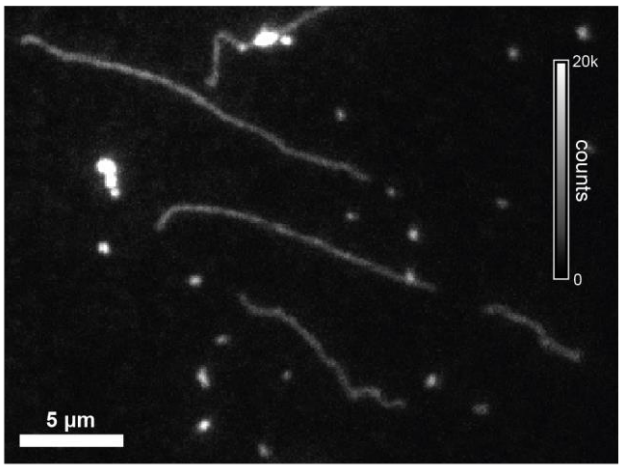

Fig. S4. Polymers experiencing flow. Local fluid flow aligns and stretches the polymers.

Analysis of AFM images of BTA polymers

The height and width of three polymers was measured from AFM images. For each polymer, the height and width is determined from Gaussian fits to cross sections along the polymer backbone. The height is defined as the amplitude of the Gaussian fit and the width as the full-width-at-half-maximum (FWHM). The polymers and distributions of the height and width determined from these polymers are shown in Fig. S5a-c. The difference in height and width between polymers depends on the polymer itself, local surface interactions, the applied force and the used AFM tip. The mean height and width as determined from these polymers varies significantly between polymers, here we measure heights of 1.3 ± 0.3 nm (a), 3.0 ± 0.4 nm (b) and 4.5 ± 0.7 nm (c) and widths of 11 ± 4 nm (a), 20 ± 6 nm (b) and 27 ± 8 nm (c), respectively. Variations in height and width are due to variations in applied force, AFM tip diameter, local differences in hydrophobicity of the surface and polymer-to-polymer variations.

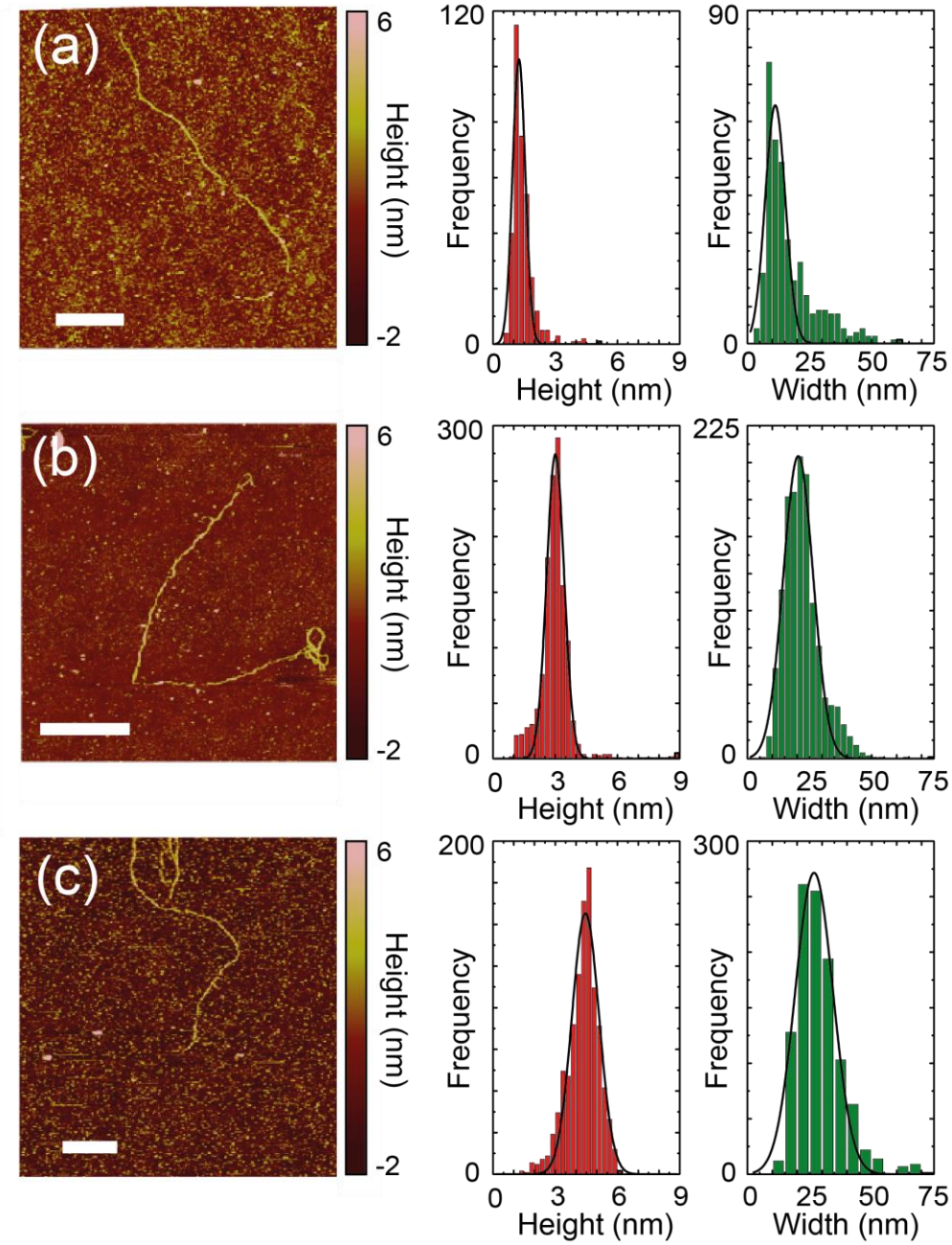

Fig. S5. Height and width analysis from AFM images. Height (red) and width (green) distributions are shown for three polymers (a-c) and were determined from Gaussian fits to cross sections along the polymer length. This yields heights of 1.3 ± 0.3 nm (a), 3.0 ± 0.4 nm (b) and 4.5 ± 0.7 nm (c) and widths of 11 ± 4 nm (a), 20 ± 6 nm (b) and 27 ± 8 nm (c). Scale bars in (a-c) are 1 µm, error bars in (d-e) are standard deviations.

To image the BTA polymers we use peak-force tapping mode, where the AFM tip (2 nm tip radius, stiffness k = 0.07 – 0.7 Nm) is modulated with a maximum force of 200 pN as feedback.BTA polymers immobilized on a glass coverslip are fragile, when performing AFM measurements part of the polymer is damaged in the first or subsequent scans as shown in Fig. S6a-d. Arrows indicate regions where the polymers are damaged. AFM measurements also seem to influence the polymer height in some cases as evidenced by the height and width of three regions for multiple scans. The height and width was determined by fitting a Gaussian function to a distribution of the height and width determined from Gaussian fits to cross sections along the polymer indicated by the shaded regions (1), (2) and (3). The height of the polymer decreases (Fig. S6e) for region (2) and (3), but remained constant in region (1). The width (Fig. S6f) increases in regions (2) and (3) and decreases again. For region (1) the width remains constant. This suggests AFM measurements influence the shape of the polymers, but the degree of influence varies between regions and polymer.

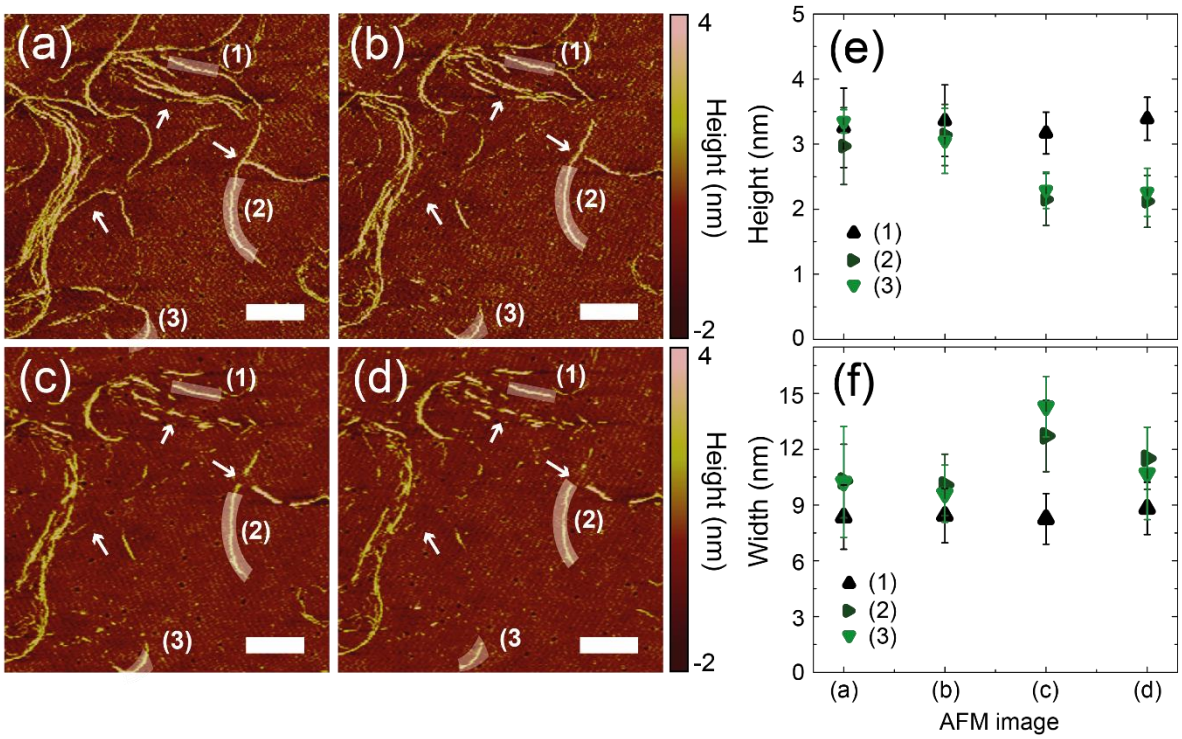

Fig. S6. Sample fragility and damage. (a-d) Four sequential AFM images of the same area showing multiple BTA polymers. Arrows indicate parts of polymers being swept away. Dashed lines indicate polymer cross sections shown in (e-g). Scale bars are 250 nm. Images were scanned with MSNL-A tips from Bruker (2 nm diameter, *k*=0.07 Nm) at 500 pN. Gaussian fit to cross sections taken from (a-d) at three different locations show a decrease in polymer height (e) and a slight increase in polymer width (f), suggesting that the AFM tip deforms the polymers.

Distribution of apparent persistence lengths

Polymers are single and unentangled when their coefficient of variation CV, i.e. the ratio of the background-corrected standard deviation of the intensity to the mean of the intensity, is below the chosen threshold. The distribution of apparent persistence lengths for these polymers is shown in Fig. S7, together with the distribution of apparent persistence lengths of polymers that were discarded due to a CV above the threshold, which is correlated to entanglement or clustering.

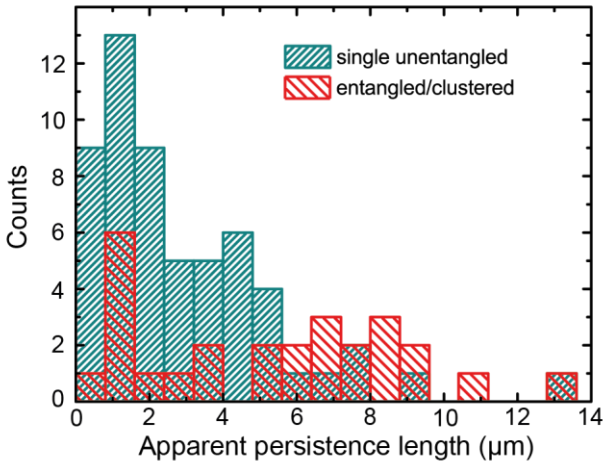

Fig. S7. Distribution of apparent persistence lengths of single unentangled (green) and entangled or clustered polymers (red). Median values of the persistence length are 2.2 ± 1.4 µm and 5.7 ± 3.5 µm, respectively.

Comparison of persistence lengths

In Fig. S8 the persistence lengths of ssDNA (5), dsDNA (6), actin (7) and microtubules (8) are compared to the persistence length of BTA (2.2 µm).

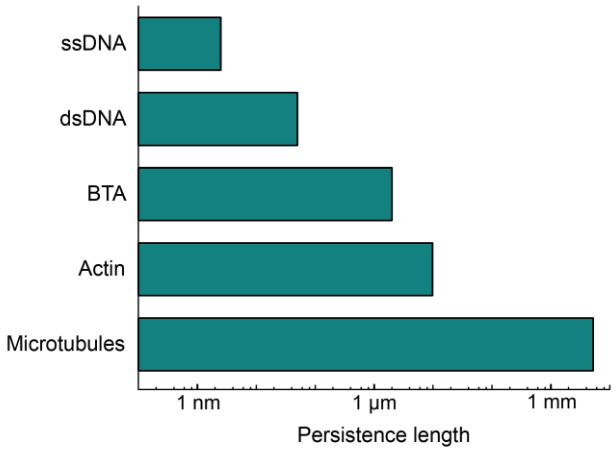

Fig. S8. Persistence lengths of different biological supramolecular polymers and BTA.

References

1. Kratny, O. and G. Porod. 1949. Röntgenuntersuchung gelöster Fadenmoleküle. *Rec. Trav. Chim. Pays-Bas.* 68:1106-1123.
2. Broedersz, C.P. and F.C. MacKintosh. 2014. Modeling semiflexible polymer networks. *Rev. Mod. Phys.* 86:995-1036.
3. Graham, J.S., B.R. McCullough, H. Kang, W.A. Elam, W. Cao, and E.M. de La Cruz. 2014. Multi-platform compatible software for analysis of polymer bending mechanics. *PLoS One* 9(4):e94766.
4. Press, W.H., S.A. Teukolsky, W.T. Vetterling, and B.P. Flannery. 1988. *Numerical recipes in C: the art of scientific computing,* 2nd ed., Cambridge university press, New York, NY, USA.
5. Murphy, M.C., I. Rasnik, W. Cheng, T.M. Lohman, and T.J. Ha. 2004. Probing single-stranded DNA conformational flexibility using fluorescence spectroscopy. *Biophys. J.* 86:2530-2537.
6. Hagerman, P.J. 1988. Flexibility of DNA, *Ann. Rev. Biophys. Biophys. Chem.* 17:265-86.
7. McCullough, B.R., L. Blanchoin, J-L. Mariel, and E.M. de La Cruz. 2008. Cofilin increases the bending flexibility of actin filaments: implications for severing and cell mechanics. *J. Mol. Biol.* 381:550-558.
8. Gittes, F., B. Mickey, J. Nettleton, and J. Howard. 1993. Flexural rigidity of microtubules and actin filaments measured from thermal fluctuations in shape. *J. Cell Biol.* 120:923-934.